JET STABILITY AND THE GENERATION OF SUPERLUMINAL AND STATIONARY COMPONENTS

IVÁN AGUDO,[1] JOSÉ-LUIS GÓMEZ,[1] JOSÉ-MARÍA MARTÍ,[2] JOSÉ-MARÍA IBÁÑEZ,[2] ALAN P. MARSCHER,[3]
ANTONIO ALBERDI,[1] MIGUEL-ANGEL ALOY,[4] AND PHILIP E. HARDEE[5]

ABSTRACT

We present a numerical simulation of the response of an expanding relativistic jet to the ejection of a superluminal component. The simulation has been performed with a relativistic time-dependent hydrodynamical code from which simulated radio maps are computed by integrating the transfer equations for synchrotron radiation. The interaction of the superluminal component with the underlying jet results in the formation of multiple conical shocks behind the main perturbation. These trailing components can be easily distinguished because they appear to be released from the primary superluminal component instead of being ejected from the core. Their oblique nature should also result in distinct polarization properties. Those appearing closer to the core show small apparent motions and a very slow secular decrease in brightness and could be identified as stationary components. Those appearing farther downstream are weaker and can reach superluminal apparent motions. The existence of these trailing components indicates that not all observed components necessarily represent major perturbations at the jet inlet; rather, multiple emission components can be generated by a single disturbance in the jet. While the superluminal component associated with the primary perturbation exhibits a rather stable pattern speed, trailing components have velocities that increase with distance from the core but move at less than the jet speed. The trailing components exhibit motion and structure consistent with the triggering of pinch modes by the superluminal component. The increase in velocity of the trailing components is an indirect consequence of the acceleration of the expanding fluid, which is assumed to be relativistically hot; if observed, such accelerations would therefore favor an electron-positron (as opposed to proton rest mass) dominated jet.

Subject headings: galaxies: jets — hydrodynamics — methods: numerical —
radiation mechanisms: nonthermal — relativity

1. INTRODUCTION

The computation of the synchrotron radio emission (Gómez et al. 1995, 1997; Hughes, Duncan, & Mioduszewski 1996; Komissarov & Falle 1996) from time-dependent relativistic hydrodynamical codes (Martí, Müller, & Ibáñez 1994; Duncan & Hughes 1994; Koide, Nishikawa, & Mutel 1996) has proven to be a powerful method to understand the physics of jets in active galactic nuclei and microquasars, improving on previous idealized analytical calculations (Marscher & Gear 1985; Hughes, Aller, & Aller 1985). Superluminal components have been studied using such formulations by introducing perturbations in the jet inlet and analyzing the resulting shock waves and their subsequent evolution along the jet (Gómez et al. 1997; Mioduszewski, Hughes, & Duncan 1997). Fluctuations in the internal structure of the shocked material may be amplified by time delay effects, resulting in a knotty brightness distribution of the superluminal component associated with the shocked plasma (Gómez et al. 1997).

In this Letter, we explore the instabilities produced in the jet resulting from the evolution of strong perturbations generated at the jet inlet. In particular, we describe a mechanism, which should be common in jets, that generates multiple superluminal as well as quasi-stationary components.

[1] Instituto de Astrofísica de Andalucía, CSIC, Apartado 3004, 18080 Granada, Spain; ivan@iaa.es, jlgomez@iaa.es, antxon@iaa.es.

[2] Departamento de Astronomía y Astrofísica, Universidad de Valencia, 46100 Burjassot (Valencia), Spain; jose-maria.marti@uv.es, jose.m.ibanez@uv.es.

[3] Institute for Astrophysical Research, Boston University, 725 Commonwealth Avenue, Boston, MA 02215; marscher@bu.edu.

[4] Max-Planck-Institut für Astrophysik, Karl-Schwarzschild-Strasse 1, D-85748 Garching, Germany; maa@mpa-garching.mpg.de.

[5] Department of Physics and Astronomy, University of Alabama, Tuscaloosa, AL 35487; hardee@athena.astr.ua.edu.

2. GENERATION OF TRAVELING PERTURBATIONS IN RELATIVISTIC JETS

Our study relies on a relativistic, axially symmetric jet model obtained by means of a high-resolution shock capturing scheme to solve the equations of relativistic hydrodynamics in cylindrical coordinates. The code is the same as that used by Gómez et al. (1997). Details of the code and its performance (equations, finite-difference approximation, and testing) can be found in Martí et al. (1997 and references therein).

The steady jet model is the same as model PM in Gómez et al. (1997), computed with a spatial resolution in both radial and axial directions of eight cells/R_b (where R_b is the beam radius at the injection position), but twice as long (covering $400R_b \times 10R_b$). It corresponds to a pressure-matched, diffuse ($\rho_b/\rho_a = 10^{-3}$), relativistic ($\Gamma_b = 4$) beam with Mach number $M_b = 1.69$. Here ρ is the proper rest-mass density and Γ is the bulk Lorentz factor; subscripts a and b refer, respectively, to atmosphere and beam; values correspond to the injection position. By allowing the jet to propagate through an isothermal atmosphere with a decreasing pressure gradient, we have induced a small opening angle in the jet (~0°3).

2.1. *Dynamics of the Main Perturbation*

We concentrate our attention on the evolution of the flow after the introduction of a square-wave perturbation at the jet inlet. This perturbation consists of an increase in the bulk Lorentz factor from the quiescent value of $\Gamma_b = 4$ to $\Gamma_p = 10$ and an increase in pressure by a factor of 2. The perturbation lasts for a time $\tau_p = 0.75R_b/c$ (where c is the speed of light), after which the jet inlet was set to the quiescent values in both Lorentz factor and pressure. The fluid piles up in front of the velocity perturbation, creating a fast shocked state. Given the
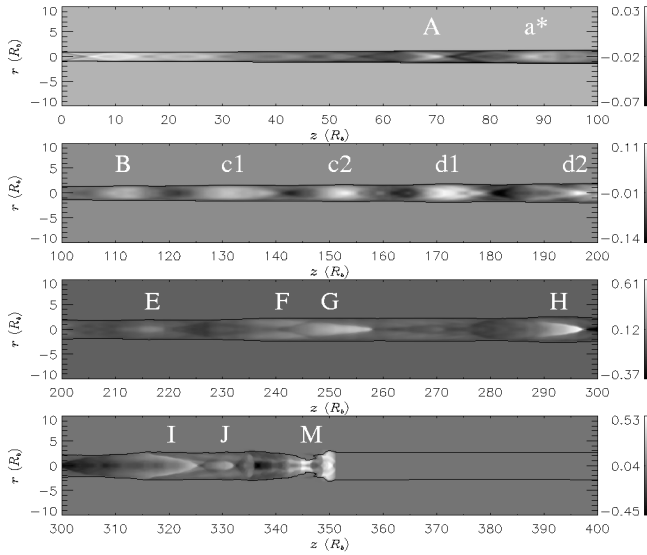
FIG. 1.—Relative variation with respect to the undisturbed steady jet of the Lorentz factor (logarithmic scale) at $t = 350R_b/c$. Note the different scale ranges in each frame to enhance the representation of the trailing conical shocks (labeled A–J) following the main perturbation (M). Typical shock angles to the jet axis are ~10°–15°.
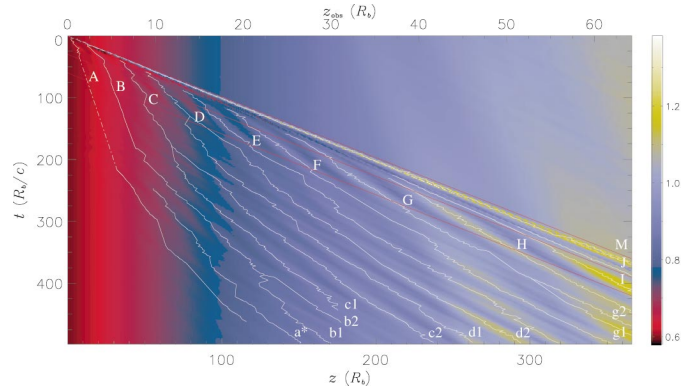

FIG. 2.—Space-time diagram for the logarithm of the jet Lorentz factor distribution. The diagonal white line from top left to bottom right marks the trajectory of the main perturbation (M), whereas the remaining white lines correspond to the tracks of the trailing shocks (identified as local maxima at positions where the Lorentz factor is 1% or more higher than the steady jet model). Red lines correspond to constant observer times $t_{obs} = 0R_b/c$, $30R_b/c$, and $60R_b/c$ for a viewing angle of 10°.

large initial shock velocity of ~0.995 ($\Gamma = 10$), in order to determine relative variations in this velocity on the order of 10% (for example, to discern between a shock Lorentz factor of 10 and, say, 11), the relative error in the calculation of the distance traveled by the shock must be smaller than 1/1000. This precision can be obtained only by studying the evolution of the shock over more than 1000 computational cells. Given the fact that the shock front is spread over three to four cells and the computational domain covers 3200 cells, only mean shock speeds (of $0.995c$) can be obtained. In general, the Lorentz factor of the leading shock should be larger than that of the preshock flow (~4 at $z = 0$; ~12 at $z = 400R_b$). This shocked state is followed by a more slowly moving (mean speed of $0.973c$) rarefaction, where the fast flow separates from the slower upstream flow. This difference in speeds stretches the perturbation along the axis. Any similar strong *supersonic* perturbation should lead to a similar shock/rarefaction structure.

The passage of the main perturbation triggers a local pinch instability that propagates behind the main perturbation, leading to the formation of a series of conical "trailing shocks" following the main perturbation (Fig. 1). Shocked and rarefied parts of the main perturbation and variation in the beam radius can be seen in the figure. The trailing structures are spaced by ~$8R_b$ for $15 < z/R_b < 55$ and ~$20R_b$ for $105 < z/R_b < 180$.

Although the type of perturbation introduced at the jet inlet is somewhat arbitrary, the qualitative results we obtain are not a function of the particular perturbation chosen; formation of trailing shocks is a general consequence of the propagation of strong perturbations through jets (see also Gómez et al. 1997, where trailing shocks appear in the hydrodynamical simulations for a different jet inlet perturbation). Further research would be of interest to quantify the physics of the trailing shocks, depending on the type of perturbation introduced, as well as the jet/external medium hydrodynamical properties.

A local solution of the dispersion relation for the pinch modes of this relativistic jet and a computation of the pinch mode structure (see Hardee et al. 1998; Hardee 2000) indicate that observed features are primarily related to the triggering of the first pinch body mode. Features in Figure 1 in the range $15 < z/R_b < 180$ have spacings between the longest unstable wavelength λ^l and the shorter maximally unstable wavelength λ^* of the first pinch body mode. The wavelengths λ^l and λ^* increase from $13R_b$ to $125R_b$ and from $4R_b$ to $19R_b$, respectively, as z increases from $0R_b$ to $250R_b$.

2.2. Evolution of the Trailing Shocks

The observed time evolution of the trailing shocks can be followed in Figure 2, which displays a space-time diagram of the Lorentz factor distribution in the jet. Trailing shocks emerge from the rarefactions that follow the main perturbation and are generated over a range of velocities and separations. The velocities are significantly smaller than the velocity of the main perturbation (and the bulk flow speed) and increase with distance from the inlet, as do the separations. Table 1 summarizes the positions, separations, and speeds of the trailing components for different observer times. In particular, consider time $t_{obs} = 60$ when the shock spacing from component A to H ranges from ~$17R_b$ to ~$76R_b$ and the shock velocity ranges from ~$0.13c$ to ~$0.69c$ for locations from $z/R_b = 12.7$ to $z/R_b = 290.9$. The separation and speed are explained by rapid passage of the main perturbation, which triggers the first pinch body mode at a wavelength whose group velocity is comparable to the rarefaction speed, $v_{gp} \sim 0.973c$. This wavelength ranges from $\lambda \sim 23R_b$ at $z/R_b \sim 50$ to $\lambda \sim 60R_b$ at $z/R_b \sim 250$. Subsequently, the perturbation slows to the wave speed v_{ph} of this wavelength. The wave speed ranges from ~$0.2c$ at $z/R_b \sim 50$ to ~$0.6c$ at $z/R_b \sim 250$. The wave speed is low for perturbations created with wavelength near λ^l (occurs at small z) and higher for perturbations created with wavelength above λ^l (occurs at larger z). Another result is that perturbations created at small z (relatively short wavelength) accelerate as they move to larger z (see Fig. 2), where their wave speed is higher.

3. EMISSION RESULTS

We have computed the synchrotron radiation from the hydrodynamical model discussed in the preceding section following the procedure described in Gómez et al. (1997 and references therein). Figure 3 shows the computed total intensity image obtained for an optically thin observing frequency. Sev-

TABLE 1
Positions, Separations, and Speeds of the Trailing Shocks in the Source Frame at Selected Observer Times[a]

Component	z(R_b)				Δz(R_b)			v(c)	v̄(c)	
	15	30	50	60	15	30	60	15	15–30	30–60
A	6.6	8.0	11.1	12.7	...	...	...	0.25	0.08	0.13
B	23.2	25.4	28.4	30.1	16.6	17.4	17.4	0.30	0.13	0.13
C	38.5	42.1	50.8	49.7	15.3	16.7	19.6	0.25	0.20	0.20
D	57.7	63.8	78.3	80.0	19.2	21.7	31.3	0.50	0.29	0.29
E	75.6	89.4	106.9	116.7	17.9	25.6	36.7	0.85	0.48	0.48
F	103.4	116.7	144.3	158.7	27.8	27.3	42.0	0.82	0.46	0.59
G	141.4	170.5	194.9	214.8	38.0	53.8	56.1	...	0.74	0.60
H	...	225.5	268.1	290.9	...	76.1	76.1	...	...	0.69
I	...	299.1	357.3	393.3	...	73.6	102.5	...	...	0.77
J	...	375.4	...	...	...	76.3	...	...	...	...

Note.—$t_{obs} = 15R_b/c$ is representative of the trailing shocks soon after their production; $t_{obs} = 30R_b/c$ and $60R_b/c$ are the times chosen to identify secondary shocks and emission components; z represents the distance along the jet axis; Δz is the distance from the previous trailing shock; v and $\bar{v}$ are, respectively, the speed and mean speed of the perturbation in the times and periods considered.

[a] Observer times t_{obs} are in units of R_b/c.

eral components are seen, corresponding to the trailing conical shocks of Figures 1 and 2, and are labeled accordingly. Typical high-frequency VLBI observations provide dynamic ranges on the order of 200 : 1 (defined as the intensity ratio of the peak to the lowest believable feature) or larger, depending on the frequency of observation and array used. All components seen in Figure 3 are above this limit and therefore are expected to be detected by actual VLBI observations.

Figure 4 displays the mean intensity along the observed jet in a space-time diagram. Trailing components have been identified across epochs, and their mean intensity peak is traced as a function of the observer's time. Almost all the trailing shocks in Figure 2 can be identified with radio components in Figure 4 and have been labeled accordingly. In Figure 4, we can distinguish a strong component associated with the main shock, followed by a jet region with low emission corresponding to the rarefaction that follows the main shock. Trailing components are observed to emerge upstream from this dip in emission. Therefore, trailing components can be easily distinguished from those generated at the jet inlet; they emanate not from the core, but rather seem to appear spontaneously downstream, created in the wake of strong perturbations. The main component is observed to move with a superluminal apparent speed that slowly decreases from ~7c to ~6c. Note that from these velocities we can infer a Lorentz factor for the hydrodynamical component between 7.3 and 6.1 (for a viewing angle of $\theta = 10°$), smaller than the value of ~10 estimated from the hydrodynamics. This apparent discrepancy may be explained by considering the time delays that severely affect the leading component, stretching its size in the observer's frame by a factor of $\beta \sin \theta/(1 - \beta \cos \theta)$. Small changes in the brightness distribution from the front to the back

of the component would then lead to a lag of the centroid behind the shock front and therefore to a slower value of its proper motion as derived from VLBI images than that expected from the velocity of the leading shock.

As observed in Figure 4, the flux densities and apparent motions of the trailing components depend strongly on the distance from the core at which they are generated, reflecting the hydrodynamics of the secondary features. Those components appearing close to the core show subluminal motions as well as flux densities that decrease very slowly with time. Components appearing farther downstream show progressively larger apparent motions (episodically superluminal) as well as weaker flux densities, rendering their detection more difficult. Table 2 compiles positions and speeds, in the observer's frame, of the trailing components at selected observer times. The values of z_{obs} for each component in Table 2 can be readily compared with those of z in Table 1 once projection effects have been removed ($z_{obs} = z \sin 10°$). All the distances of emission components match positions of peaks in Lorentz factor within an error smaller than 16%, except for components I and J. A similar comparison can be made between the mean apparent speeds in the intervals $t_{obs} = 15–30$ and 30–60 and the true
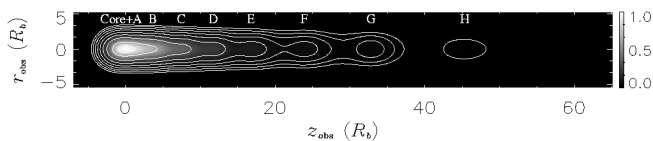

Fig. 3.—Simulated total intensity radio map (convolved with a beam of $2.2R_b$ FWHM) for epoch $50R_b/c$ in the observer's frame and a viewing angle of 10°. Contours are plotted for 0.5, 1, 2, 4, 8, 16, 32, 64, and 90 percent of the normalized peak intensity of the core. Components have been labeled except for I, J, and M (associated with the main perturbation), which have already propagated off the plot to the right.
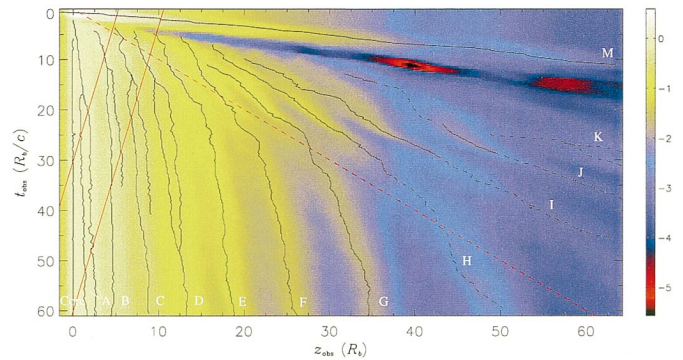

Fig. 4.—Space-time diagram for the logarithm of the mean (unconvolved) intensity (across slices normal to the jet axis and normalized to the mean core intensity) in the observer's frame. Black tracks correspond to trajectories of emission components associated with the main perturbation (M) and the trailing components. Black dashed lines correspond to components with intensities below 0.5% of the normalized value. Red solid lines are lines of constant time in the source frame (*from left to right*: $t = 30R_b/c$, $60R_b/c$). The red dashed line represents a speed equal to c.

TABLE 2
Observer's Frame Positions and Speeds of the Trailing
Components at Selected Observer Times[a]

| | $z_{obs}(R_b)$ | | | | $v_{obs}(c)$ | $\bar{v}_{obs}(c)$ | |
Component	15	30	50	60	15	15–30	30–60
A	1.0	1.5	1.9	2.2	0.16	0.03	0.05
B	4.4	5.1	4.7	4.5	0.20	0.05	0.00
C	7.1	8.0	8.7	8.8	0.41	0.06	0.03
D	9.8	11.4	12.8	13.3	0.53	0.11	0.08
E	12.9	16.6	18.0	18.8	0.41	0.25	0.07
F	16.0	22.1	24.7	25.9	0.57	0.41	0.12
G	19.6	28.0	33.7	34.7	0.41	0.56	0.22
H	22.9	36.1	44.5	50.7	0.57	0.88	0.49

[a] Observer times t_{obs} are in units of R_b/c.

speeds in Table 2, although in this case the agreement is within 30%. The higher velocities of components I and J result in longer time delays, which stretches their emitting volume in the observer's frame, thus rendering the determination of their positions more difficult.

4. DISCUSSION AND CONCLUSIONS

Our relativistic hydrodynamic simulations show that the passage of a strong perturbation along a jet triggers instabilities caused by pressure mismatches between the jet and external medium, leading to the formation of conical trailing recollimation shocks. The existence of these features has been ignored in previous analyses in which analytical square-wave shock approximations have been used. Computation of the synchrotron emission reveals that these trailing components should be detectable with present VLBI arrays.

Our simulations show that trailing components should appear to emerge in the wake of strong components rather than to be ejected from the core. They are generated with a wide range of apparent speeds, from almost stationary (near the core) to superluminal—although slower than the main leading feature—farther down the jet. They are conical (more generally oblique in three-dimensional models) shocks and hence should exhibit polarization properties that depend on the viewing angle (Cawthorne & Cobb 1990) and are different from those of the main components. Evidence for the existence of trailing components has been found in the radio galaxy 3C 120, whose jet contains a standing component whose flux density is observed to be enhanced after the passage of a very strong superluminal component (Gómez et al. 2000). Recent high-resolution 7 mm Very Long Baseline Array observations (Jorstad et al. 2001) have revealed the existence of steady

components close to the core in a large number of γ-ray bright blazars; these may be associated with trailing components.

The superluminal component corresponding to the main perturbation in our simulation exhibits a rather constant pattern speed, even though the underlying fluid velocity is observed to accelerate significantly. Therefore, the observation of the proper motions of superluminal components may not detect any actual acceleration of the jet fluid. However, our simulations show that trailing components should appear to accelerate, reflecting acceleration of the fluid. If such accelerations are not observed, this would indicate that the fluid is not relativistically hot, as expected for an electron-positron plasma. In this case, the internal energy of the jet could be inferred to have an energy density dominated by the rest mass of nonrelativistic protons.

From our analysis, we conclude that jets and, by implication, the accretion process onto the central black hole can be steadier than previously thought while still producing highly variable emission and prolific production of superluminally moving knots. Multiple components in radio maps can be produced by a single ejection event.

The mechanism of production of these trailing components is a general characteristic of nonsteady supersonic jet flows, i.e., not specific to relativistic dynamics. It could be applied to other astrophysical scenarios such as outflows from young stellar objects where very knotty jets are found with series of components moving at very different speeds from those inferred for the fluid flow (Xu, Hardee, & Stone 2000).

The spacing and acceleration of the trailing components can be understood as resulting from the triggering of pinch modes by the main perturbation. Pinch wavelengths with group velocity comparable to the speed of the rarefaction associated with the main perturbation are excited but then decelerate to the phase speed of the dominant wavelength. The excited wavelength is longer and the wave speed is higher at larger distance as an indirect consequence of the acceleration of the expanding jet.

REFERENCES

Cawthorne, T. V., & Cobb, W. K. 1990, ApJ, 350, 536
Duncan, G. C., & Hughes, P. A. 1994, ApJ, 436, L119
Gómez, J. L., Marscher, A. P., Alberdi, A., Jorstad, S. G., & García-Miró, C. 2000, Science, 289, 2317
Gómez, J. L., Martí, J. M., Marscher, A. P., Ibáñez, J. M., & Alberdi, A. 1997, ApJ, 482, L33
Gómez, J. L., Martí, J. M., Marscher, A. P., Ibáñez, J. M., & Marcaide, J. M. 1995, ApJ, 449, L19
Hardee, P. E. 2000, ApJ, 533, 176
Hardee, P. E., Rosen, A., Hughes, P. A., & Duncan, G. C. 1998, ApJ, 500, 599
Hughes, P. A., Aller, H. D., & Aller, M. F. 1985, ApJ, 298, 301
Hughes, P. A., Duncan, G. C., & Mioduszewski, A. J. 1996, in ASP Conf. Ser. 100, Energy Transport in Radio Galaxies and Quasars, ed. P. E. Hardee, A. H. Bridle, & J. A. Zensus (San Francisco: ASP), 137

Jorstad, S. G., Marscher, A. P., Mattox, J. R., Wehrle, A. E., Bloom, S., & Yurchenko, A. V. 2001, ApJS, in press
Koide, S., Nishikawa, K., & Mutel, R. L. 1996, ApJ, 463, L71
Komissarov, S. S., & Falle, S. A. E. G. 1996, in ASP Conf. Ser. 100, Energy Transport in Radio Galaxies and Quasars, ed. P. E. Hardee, A. H. Bridle, & J. A. Zensus (San Francisco: ASP), 165
Marscher, A. P., & Gear, W. K. 1985, ApJ, 298, 114
Martí, J. M., Müller, E., Font, J. A., Ibáñez, J. M., & Marquina, A. 1997, ApJ, 479, 151
Martí, J. M., Müller, E., & Ibáñez, J. M. 1994, A&A, 281, L9
Mioduszewski, A. J., Hughes, P. A., & Duncan, G. C. 1997, ApJ, 476, 649
Xu, J., Hardee, P. E., & Stone, J. M. 2000, ApJ, 543, 161